








Cite this: *Nanoscale*, 2024, **16**, 20968

# Nanoplasmonic sensing to study CO and oxygen adsorption and CO oxidation on size-selected Pt<sub>10</sub> clusters†

Benjamin Demirdjian, <sup>a</sup> Mykhailo Vaidulych, <sup>b</sup> Igor Ozerov, <sup>a</sup> Frédéric Bedu,<sup>a</sup> Štefan Vajda <sup>b</sup> and Claude R. Henry <sup>a</sup>

The adsorption of CO and oxygen and CO oxidation on size-selected Pt<sub>10</sub> clusters were studied by indirect nanoplasmonic sensing (INPS) in the pressure range of 1–100 Pa at  $T = 418$  K. CO adsorption was reversible, inducing a blue-shift in the localised surface plasmon resonance (LSPR) response, regardless of the initial CO pressure. We observe a plateau at approximately  $\Delta\lambda = -0.1$  nm at  $P_{\text{CO}} > 2.7$  Pa, indicating saturation of CO adsorption on Pt<sub>10</sub> clusters. Oxygen induces both chemisorption and oxidation of Pt<sub>10</sub> clusters until a regime is reached where  $\Delta\lambda_{\text{max}}$  remains positive and constant, showing that the Pt<sub>10</sub> clusters are completely oxidised. CO oxidation at different molar fractions is also followed by INPS. All results are discussed in relation to our previous works on 3 nm Pt nanocubes [B. Demirdjian, I. Ozerov, F. Bedu, A. Ranguis and C. R. Henry, *ACS Omega*, 2021, **6**, 13398–13405]. The study demonstrates the suitability of INPS towards the understanding of the nature and function of matter in the largely unexplored subnanometer size regime where properties can often dramatically change when altering the particle size by a single atom.

Received 28th June 2024,  
Accepted 7th October 2024

DOI: 10.1039/d4nr02682a

rsc.li/nanoscale

## 1. Introduction

Model catalysts consist of metal clusters or nanoparticles supported on an oxide surface. They are usually studied in detail using surface science techniques under UHV.<sup>1</sup> However, catalytic activity studies are mostly limited to very low pressures (below  $10^{-4}$  Pa), which is far from the working pressure of real catalysts (100 Pa to 100 kPa range). This fact is known as the ‘pressure gap’ in fundamental catalytic studies.<sup>2</sup> Recently, new techniques have been developed to fill this gap, such as polarisation modulation infrared reflection absorption spectroscopy (PM-IRAS),<sup>3</sup> sum frequency generation spectroscopy (SFG),<sup>4</sup> and near ambient pressure XPS.<sup>5</sup> These techniques work well in the 100 Pa range (or in some cases up to atmospheric pressure) with metal particles supported on a single crystal surface and are expensive. A more recent technique called indirect nanoplasmonic sensing (INPS) has been developed to study adsorption and catalytic reactions on supported particles.<sup>6</sup> This technique can be used at any pressure and is rela-

tively inexpensive. The principle is based on the adsorption of gases onto catalytic metal particles, which changes the dielectric properties at their surface and produces a shift in the LSPR wavelength of the underlying Au disk sensor; this is indirect nanoplasmonic sensing, as the gold disks are covered with a 5–10 nm thick oxide film (typically silica) and there is no direct contact of gas molecules with the Au sensors. With this technique, we can follow the chemisorption of gases (CO, O<sub>2</sub>, H<sub>2</sub>, etc.) on Pt nanoparticles,<sup>6,7</sup> the CO + O<sub>2</sub> reaction on Pt nanoparticles,<sup>6,7</sup> and the H<sub>2</sub> + O<sub>2</sub> reaction on Pt and Pd nanoparticles.<sup>6,8,9</sup> In the case of bimolecular reactions, the INPS technique allowed us to follow the adsorption of the reactants during the reaction, while the reaction rate (production of CO<sub>2</sub> or H<sub>2</sub>O) could be recorded using a mass spectrometer.<sup>7,8,10</sup> The reaction rate for the exothermic reaction can also be qualitatively monitored using indirect sensing, as the increase in the temperature of the nanoplasmonic sensor due to the reaction provides an additional linear redshift as a function of the temperature increase.<sup>11</sup> In the present study, we want to investigate whether INPS is also applicable to size-selected clusters. The latter species are largely unexplored and represent an alternative to traditional powder-based catalysts, as their physical and chemical properties can be tuned in an atom by atom fashion,<sup>12</sup> while their small size allows efficient utilization of the material. The high reactivity of such clusters is given by all their undercoordinated atoms exposed to the reactants and the drastic variation

<sup>a</sup>Aix Marseille Univ, CNRS, CINAM, Marseille, France.

E-mail: benjamin.demirdjian@cnrs.fr

<sup>b</sup>Department of Nanocatalysis, J. Heyrovský Institute of Physical Chemistry v.v.i., Czech Academy of Sciences, Dolejškova 2155/3, 182 23 Prague 8, Czech Republic.

E-mail: mykhailo.vaidulych@jh-inst-cas.cz

† Electronic supplementary information (ESI) available. See DOI: <https://doi.org/10.1039/d4nr02682a>



in the density of electronic states near the Fermi level.<sup>13–15</sup> However, a comprehensive understanding of how gas molecules interact with subnanometer clusters remains a fundamental challenge due to the low sensitivity of laboratory instruments and the very small amount of cluster-based catalysts utilized. For these needs, first the sensitivity of the INPS method was improved by identifying the optimal shape of the gold disks used as base sensors and implementing a precise control over the high uniformity of these disks, prepared by electron beam lithography (EBL), by systematic comparisons between experimental absorption spectra and theoretical results from finite difference time-domain (FDTD) calculations.<sup>16</sup> Finally, we obtained very sharp plasmon peaks with a two-fold increase in intensity and a three-fold reduction in width. In order to precisely dose the amount of deposited size selected clusters, a conductive substrate needs to be used.<sup>17</sup> As such support, indium tin oxide (ITO) thin films on glass were chosen, which have the advantage of providing good adhesion for gold, thus avoiding the use of an adhesive layer (Cr or Ti) which enlarges/broadens the gold plasmon peak. The adsorption of CO and oxygen was then studied on the Pt<sub>10</sub> clusters with low surface density achieving a good INPS sensitivity in the pressure range 1–100 Pa at 418 K. At this temperature, the adsorption of CO was reversible, while oxygen adsorption did not exhibit the same behavior. However, the layer of the adsorbed oxygen could be completely removed upon exposure to CO, resulting in CO<sub>2</sub> formation as witnessed by INPS measurements.

## 2. Sample fabrication and characterisation

### 2.1 Nanofabrication protocol

The samples were fabricated using e-beam lithography, metal evaporation, and lift-off techniques. Commercially available ITO-coated glass substrates (1 mm thick, square shape, 20 × 20 mm,  $R \leq 120$  Ohm per sq) were used for sample fabrication. To ensure that the substrate surfaces were free of contaminants, we cleaned them in successive ultrasonic baths of acetone and isopropyl alcohol (IPA) for 10 minutes each, rinsed them under a stream of deionized water and dried them under clean nitrogen. The substrates were then exposed to RF-generated oxygen plasma at 150 °C for 10 minutes to enhance the adhesion of the e-beam resist layers. Two thin films of commercially available resists: ARP617.04 (PMMA with 30% of MAA co-polymer) and ARP679.02 containing PMMA in ethyl lactate were successively spin-coated at 6000 rpm and 4000 rpm for 60 seconds each and then baked on a hotplate at 200 °C and 170 °C, respectively. The mean thicknesses were calibrated separately and were approximately 150 nm for ARP617.04 and 70 nm for ARP679.02. The final thickness of the resist bilayer deposited on the samples ranged from 210 to 230 nm, as measured with a contact profilometer (Dektak XT, Bruker). Such a bilayer structure facilitates lift-off after metal deposition. A Pioneer system (Raith, Germany) was used to

selectively expose the areas of the resist to the electron beam according to the desired pattern. The acceleration voltage was 20 kV, and the exposure dose was 120  $\mu\text{C cm}^{-2}$ . Typical features were disks of 140 nm diameter organized in square arrays with a working area of 100 × 100  $\mu\text{m}$ , repeated over a total area of 2 × 2 mm.

Next, the exposed substrates were immersed in a MIBK-IPA developer solution (Allresist) for 55 seconds to remove the exposed resist areas and rinsed the substrate with IPA for 55 seconds to complete the development process. A thin layer of gold was then deposited onto the substrates using a Joule effect evaporator (Auto 306, Edwards vacuum) equipped with a quartz microbalance for thickness control. Finally, the substrates were immersed in acetone to dissolve the underlying resist layer, gently agitated to facilitate the removal of the resist and the attached metal layer, and thoroughly rinsed with a solvent and deionized water to remove any remaining residues. The thickness of the metal layers was controlled using a contact profilometer.

After fabrication, the samples were characterized by SEM and by optical absorption. The plasmonic sensor was then coated with a 6 nm thick SiO<sub>2</sub> layer by magnetron sputtering at a deposition rate of about 1.5 nm min<sup>−1</sup>.

### 2.2 Deposition of Pt<sub>10</sub> clusters

Pt<sub>10</sub> clusters with atomic precision were prepared using a cluster deposition instrument at HIPC.<sup>18</sup> The technique is based on the gas phase synthesis of the size-selected clusters utilizing a gas aggregation cluster source (GAS) of Haberland type, a system of ion guides and ion beam optics, and a quadrupole mass spectrometer (QMS). The synthesis of Pt clusters with a wide size distribution starts off in GAS by the condensation of the metal atoms produced by magnetron sputtering as the source of Pt atoms. For this need, a 2" planar magnetron was equipped with a Pt target (3 mm thick, 99.99% purity). Ar and helium with a total flow rate of 400 sccm were used as primary sputtering and carrier gases and the deposition process was initiated upon the plasma discharge ignition using MDX 500 DC power supply (Advanced Energy). Clusters with a wide size distribution were then collected and guided with conical and linear ion guide octupoles (Extrel). Transported downstream, clusters were mass filtered with a 9.5 mm tri-filter quadrupole mass spectrometer (Extrel) operating at an oscillator frequency of 440 kHz allowing effective size-selection of clusters in the mass range ( $m/z$ ) of 10–16 000 amu. QMS is then followed by a quadrupole deflector, so that in the pass-through mode, ionic clusters are directed into a channel electron multiplier for mass spectrum collection. By monitoring the mass spectrum, the GAS parameters and potentials on each lens were optimized to obtain the highest flux of Pt<sub>10</sub> clusters during deposition. After the cluster beam was bent 90° using a quadrupole bender, the size selected clusters were deposited on the gold disks covered by a silica film on the ITO film based plasmonic sensor mounted on the sample holder. Two contacts were made on the top ITO layer of the sensor so that the flux of charged clusters could be



monitored using a picoamperemeter during the deposition process. The number of deposited clusters (atoms) was recorded in real time using custom software, and the surface coverage with Pt was kept at 10% of the atomic monolayer (ML) equivalent to avoid agglomerate formation. The resulting cluster density was  $1.5 \times 10^{13}$  clusters per  $\text{cm}^2$ .

### 2.3 ITO vs. glass substrate effect

When a metallic chromium seed layer was used to increase the adhesion of Au on glass substrates, it was observed that this Cr layer degrades the LSPR signal.<sup>16</sup> Thus, we decided to search for new substrates where no adhesion layer is required and found in the literature<sup>19</sup> that ITO substrates are well suited for this purpose. Additionally, the good electrical conductivity of ITO films facilitates sample fabrication by greatly reducing the charging effects during e-beam lithography as well as during size-selected cluster deposition. We utilized commercially available ITO films sputtered onto high-quality float glass substrates (CEC 120 S windows from Präzisions Glas & Optik GmbH). We fabricated Au disks on these commercial substrates using the following parameters: diameter  $d = 140$  nm, height  $h = 17.5$  nm and pitch  $p = 300$  nm. FDTD calculations performed on such Au disks show that on the ITO substrate, the gold disks provide sharper spectra. Fig. 1 shows the simulated optical absorption spectra of the Au disk on bare glass with a Cr layer (black curve) and without any adhesion layer on ITO-coated glass (red curve). The peak obtained with the Cr layer (Au disk/Cr/glass) exhibits a blue-shift ( $\Delta\lambda = -34.4$  nm) and is broader ( $\Delta_{\text{FWHM}} = +71.2$  nm) compared to the Au disk/ITO/glass sample.

The choice of ITO substrates therefore offers two main advantages: a conductive substrate, which facilitates e-beam lithography and is required for the deposition of Pt clusters; and a sharper and more intense LSPR signal, which will enhance the sensitivity of our plasmonic sensor.

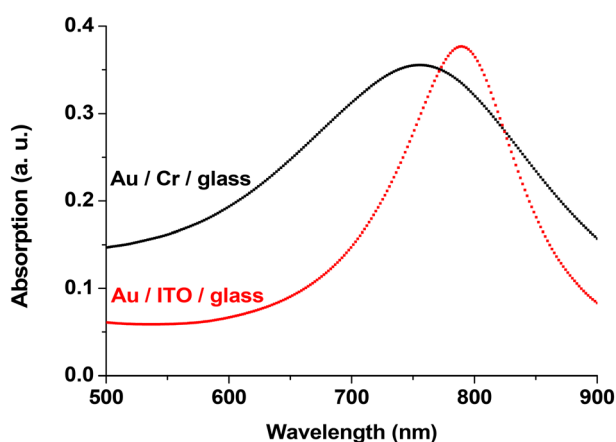


**Fig. 1** FDTD simulated LSPR responses corresponding to Au disks ( $h = 17.5$  nm,  $p = 300$  nm,  $d = 140$  nm) deposited onto an ITO-coated film (21 nm) glass window (red points) and onto a bare borosilicate glass window with a 2 nm Cr adhesion layer (black points).

### 2.4 Annealing effect

A plasmonic sample (Au disks/ITO/glass) without a  $\text{SiO}_2$  layer was thermally annealed for 3 h at  $350^\circ\text{C}$  in an oven under a flow of He ( $250 \text{ ml min}^{-1}$ ) to stabilize the microstructure and shape of the Au nanodisks.<sup>20</sup> This step is important to avoid temperature-induced irreversible spectral shifts during experiments at elevated temperatures, which can be caused by (micro)structural reshaping of the sensor particles. Typically this thermal annealing step leads to the recrystallization of the nanodisks. Fig. 2a shows that annealing induces an increase in FWHM of 20.3 nm and a blue-shift of  $\Delta\lambda = -119.0$  nm! It also causes a decrease in the average diameter of the Au disks of 23 nm ( $\Delta d = 145.5\text{--}122.5$ ) and a shape evolution, as observed by scanning electron microscopy. Fig. 3 shows the SEM images and corresponding diameter distributions before and after annealing. This means that gold material diffuses

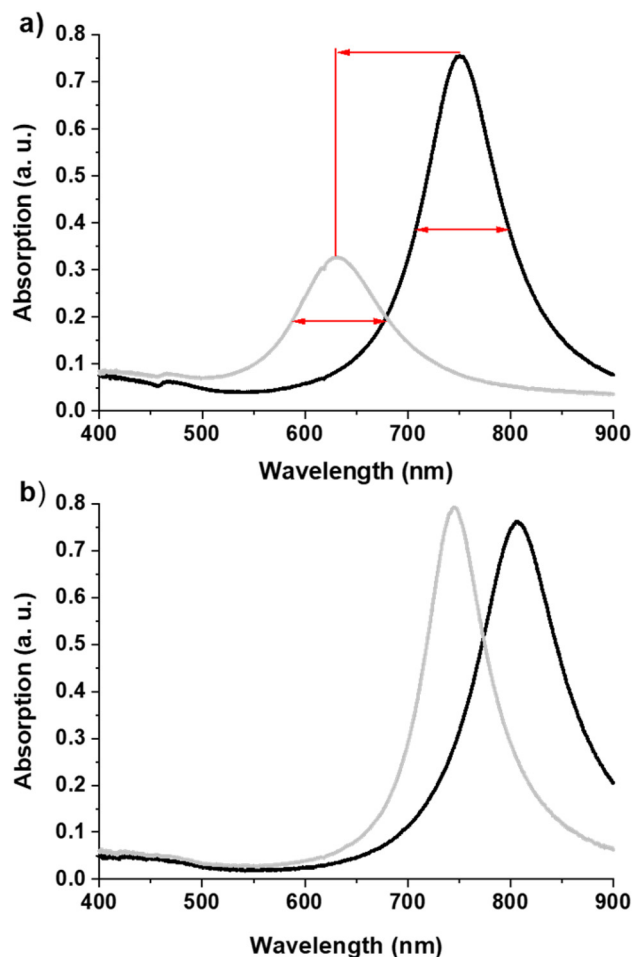


**Fig. 2** (a) Experimental LSPR responses of Au disks ( $h = 22$  nm,  $p = 300$  nm,  $d = 140$  nm) deposited onto an ITO film (21 nm) on glass window before (black points) and after (grey points) annealing at  $350^\circ\text{C}$  under He flow. (b) Experimental LSPR responses of Au disks ( $h = 17.5$  nm,  $p = 300$  nm,  $d = 140$  nm) covered by a thin  $\text{SiO}_2$  layer (6 nm) and deposited onto an ITO film (21 nm) supported on a HQ-float glass window before (black points) and after (grey points) annealing at  $350^\circ\text{C}$  under He flow.



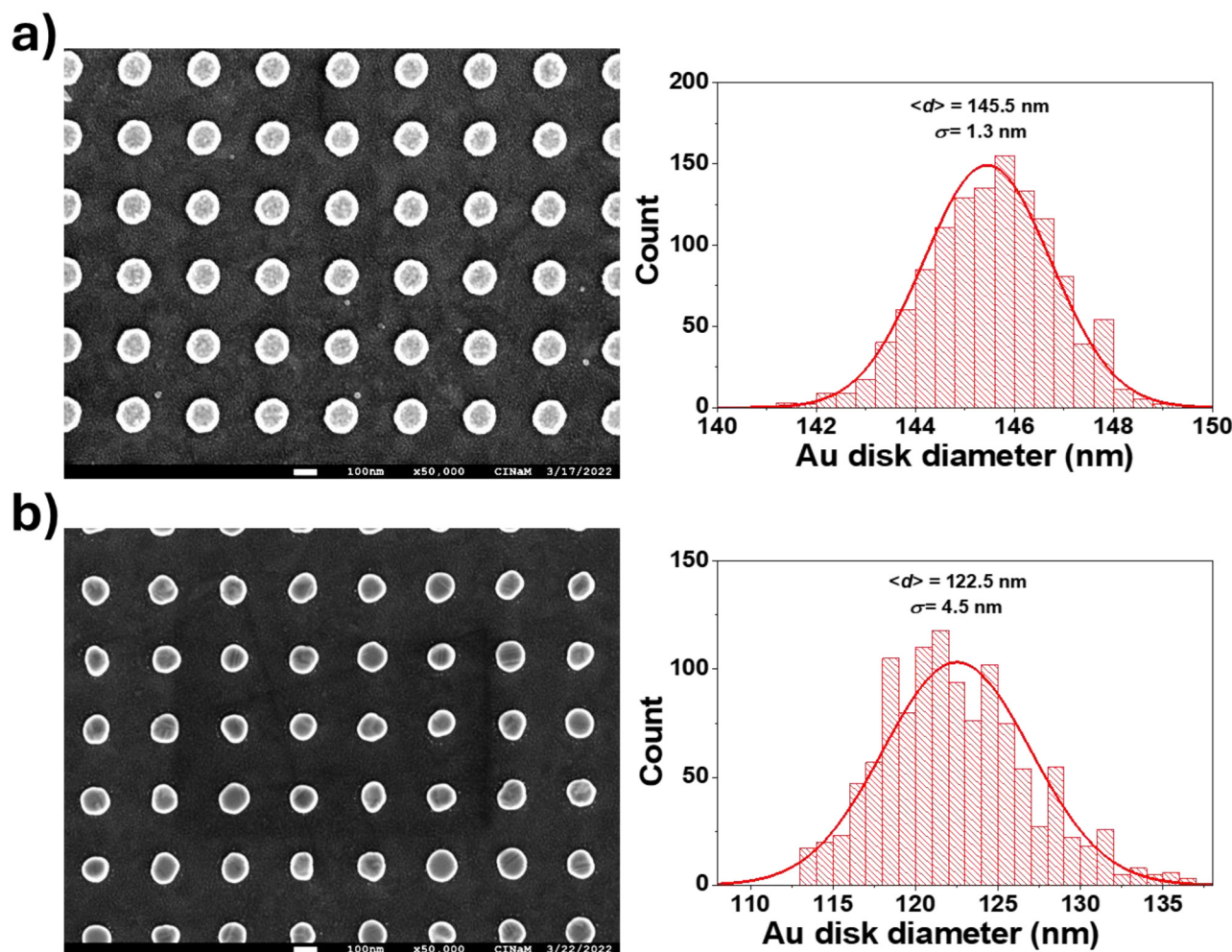


**Fig. 3** SEM images (same magnification  $\times 50\,000$ ) and disk diameter size distributions of Au disks ( $h = 17.5$  nm,  $p = 300$  nm) deposited onto an ITO-coated film (21 nm) glass window before (a) and after (b) annealing at 350 °C under He flow. SEM images were taken with a JEOL JSM-7900F.

onto and possibly into the substrate during annealing. Indeed, upon close examination of the high-magnification SEM image (Fig. 4), we observe concentric circles around the annealed Au disks, which are the footprints of the disks before annealing. With FDTD simulations, we cannot solely explain and model such a large blue-shift (Fig. 2a) based on the diameter difference alone. Therefore, we assume that the thickness, roughness and shape of the Au disks are also certainly modified during annealing. Moreover, the optical properties of ITO films can be also modified by annealing as reported by Wu *et al.*<sup>21</sup>

To minimize such significant modifications, we coated the Au disks on ITO with a SiO<sub>2</sub> layer before annealing. In this case (Fig. 2b), the observed blue-shift is smaller ( $\Delta\lambda = -61.8$  nm) and the FWHM variation is negative ( $\Delta_{\text{FWHM}} = -18.6$  nm). This comparison confirms that the SiO<sub>2</sub> layer protects and enhances the stability of the detection nanostructure at high temperatures.<sup>6</sup> Moreover, CO and oxygen do not absorb on silica layers at temperatures above 35 K, as was already shown by Collings *et al.* using temperature pro-

grammed desorption (TPD).<sup>22</sup> Thus, this has no effect on LSPR shift during CO oxidation.

### 2.5 Pt<sub>10</sub> cluster deposition: the LSPR response

The sample used for Pt cluster deposition consists of Au disks ( $h = 17.5$  nm,  $p = 300$  nm,  $d = 140$  nm) fabricated on a 21 nm thick ITO film on glass, covered with a SiO<sub>2</sub> layer (6 nm) and annealed at 350 °C under He flow. We measured LSPR responses before (black points) and after (red points) deposition of Pt<sub>10</sub> clusters (Fig. 5) and clearly observed a red-shifted LSPR response of  $\Delta\lambda = 5.8$  nm due to the Pt<sub>10</sub> clusters.

We conducted FDTD simulations [method described in ref. 16] considering the Pt clusters as 2D conductive disks with a thickness of 0.3 nm and a diameter of 1 nm. In our simulations, we considered these 2D objects with a conductivity of  $5 \times 10^5$  S m<sup>-1</sup>, which is lower than the bulk conductivity of platinum ( $9.43 \times 10^6$  S m<sup>-1</sup>). This value is close to that found in the literature for ultrathin Pt films where Agustsson *et al.*<sup>23</sup> measured  $5.7 \times 10^5$  S m<sup>-1</sup> (Fig. 3 of ref. 23) indicating a resis-





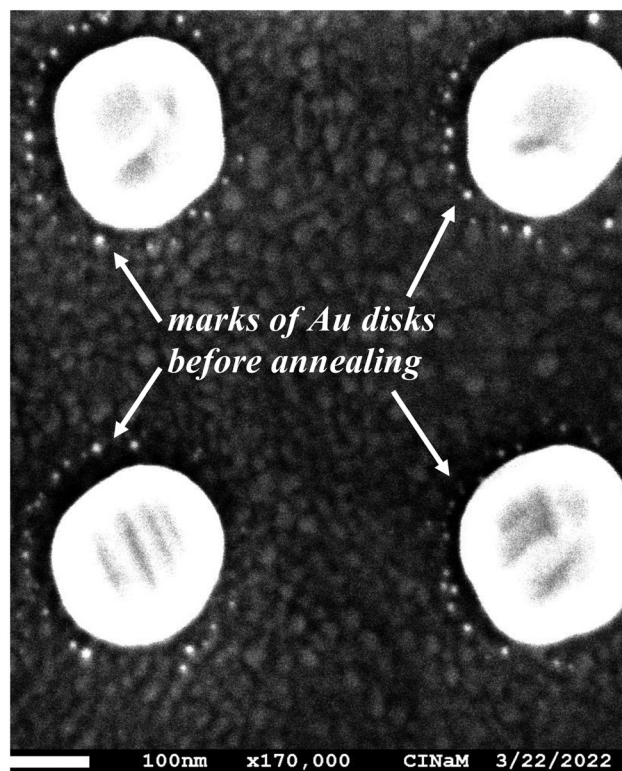


Fig. 4 High magnification ( $\times 170\,000$ ) SEM image of Au disks ( $h = 17.5$  nm,  $p = 300$  nm,  $d = 140$  nm) deposited onto an ITO-coated film (21 nm) glass window after annealing at  $350^\circ\text{C}$  under He flow. The image was taken with a JEOL JSM-7900 F.

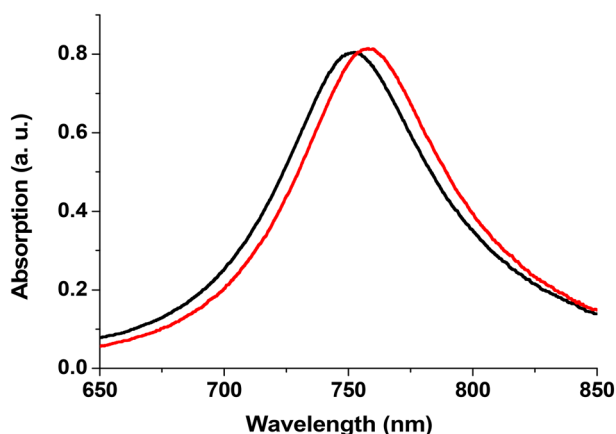


Fig. 5 Experimental LSPR responses corresponding to Au disks ( $h = 17.5$  nm,  $p = 300$  nm,  $d = 140$  nm) covered with a  $\text{SiO}_2$  layer (6 nm) deposited onto an ITO-coated film (21 nm) glass window before (black points) and after (red points)  $\text{Pt}_{10}$  cluster deposition.

tance of  $1000\ \Omega$  ( $1 \times 10^{-3}$  S) for a thin film of about 1.75 nm. We also chose a smaller Au disk diameter and thickness ( $d = 130$  nm,  $h = 15$  nm) than the experimental values in an attempt to simulate an annealing effect. We have chosen these values arbitrarily because we don't know exactly what happens

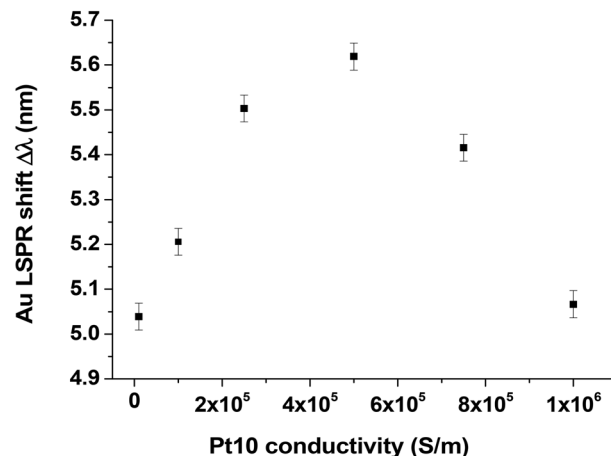


Fig. 6 FDTD simulated LSPR shifts corresponding to  $\text{Pt}_{10}$  clusters decorated Au disks ( $h = 15$  nm,  $p = 300$  nm,  $d = 130$  nm) covered with a  $\text{SiO}_2$  layer (6 nm) deposited onto an ITO-coated film (21 nm) glass window covered with  $\text{Pt}_{10}$  clusters with different 2D conductivity values.

during annealing. We certainly have a decrease in the diameter of the Au disks as there is a blue shift in the position of the LSPR response (Fig. 2b), but what about their height? We cannot measure it accurately.

Fig. 6 shows FDTD spectra obtained at different conductivities; the maximum LSPR red-shift ( $\Delta\lambda = 5.6$  nm) is obtained at a conductivity of  $5 \times 10^5\ \text{S m}^{-1}$ . This theoretical shift is in good agreement with the experimental value ( $\Delta\lambda = 5.8$  nm measured in Fig. 5).

### 3. CO and oxygen adsorption and CO oxidation

Gas sensing experiments were conducted in a homemade vacuum (HV) reactor described in detail in ref. 7. Prior to the introduction of CO and  $\text{O}_2$  gases, the reactor was pumped until a pressure  $P \leq 10^{-6}$  Pa. We define  $X_{\text{CO}}$  as the CO molar fraction given by the following equation:

$$X_{\text{CO}} = P_{\text{CO}} / (P_{\text{CO}} + P_{\text{O}_2}) \quad (1)$$

$P_{\text{CO}}$  and  $P_{\text{O}_2}$  are the partial pressures of CO and  $\text{O}_2$  gases measured inside the gas chamber with a Pirani/cold cathode transmitter (Pfeiffer-Vacuum, PKR 251). The temperature  $T$ , controlled from room temperature to 418 K, is measured inside the HV reactor with a type K thermocouple sensor. Langhammer *et al.*<sup>9</sup> depict the typical variation  $\Delta\lambda$  vs.  $T$  characteristics of the INPS sensor chip upon external heating; that is, a linear  $T$  dependence and a temperature sensitivity of  $\Delta\lambda = 0.013\ \text{nm K}^{-1}$ . In our case, we have also followed this dependence (Fig. S1, S2 and S3†) and found a sensitivity of  $\Delta\lambda = 0.02\ \text{nm K}^{-1}$ . As the introduction of gas (at RT in the gas line) into the heated HV reactor disturbs the PID controller and induces temperature instability for a few minutes, we corrected the  $\Delta\lambda$  curves for this artefact.



### 3.1 CO adsorption

To study CO adsorption, pure gas from Linde (Minican HiQ purity 3.7) was introduced into the HV reactor at  $T = 418$  K at various initial pressures.

CO molecules are adsorbed on Pt<sub>10</sub> clusters, changing the dielectric properties at the surface of the Pt<sub>10</sub> clusters and producing a shift in the LSPR wavelength of the underlying Au disk sensor, this is indirect plasmonic sensing (INPS) because the gold disks are covered with a SiO<sub>2</sub> layer and there is no direct contact of gas molecules with Au sensors.<sup>7,20</sup> For each CO pressure, we recorded UV-Vis absorption spectra every minute (see Fig. S2†) and we plotted the Au LSPR shift  $\Delta\lambda$  measured for each CO pressure after  $t = 30$  min when the sample temperature is stabilised (Fig. 7). We could observe a blueshift in the LSPR response, regardless of the initial CO pressure, ranging from 1.1 Pa to 28 Pa. We observed a plateau at approximately  $\Delta\lambda = -0.1$  nm at  $P_{\text{CO}} > 2.7$  Pa indicating saturation of CO adsorption on Pt<sub>10</sub> clusters. This blue-shift is lower than that observed in our previous work on nanometer-size cubic Pt particles.<sup>7</sup> If we calculate the number of Pt surface atoms per Au disk, we find that this number is 1.7 times higher for Pt nanocubes than for Pt<sub>10</sub> clusters. After successive adsorption measurements, the maximum shift is the same, meaning that there is no coalescence of Pt clusters induced by CO at 418 K. This is in agreement with previous GISAXS measurements showing that coalescence starts at  $T > 593$  K.<sup>24</sup>

### 3.2 Oxygen adsorption

Pure oxygen gas from Linde (Minican HiQ purity 4.5) was introduced into the HV reactor at  $T = 418$  K at  $P_{\text{O}_2} = 87$  Pa. We plotted the Au LSPR shift  $\Delta\lambda$  over time, taking measurements every 5 minutes (Fig. 8).

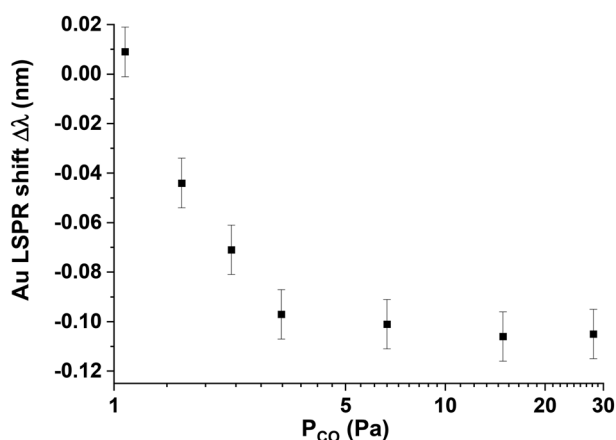


**Fig. 7** Experimental Au LSPR shifts versus  $P_{\text{CO}}$  at  $T = 418$  K for Pt<sub>10</sub> clusters deposited on Au disks ( $h = 17.5$  nm,  $p = 300$  nm,  $d = 140$  nm) covered with a SiO<sub>2</sub> layer (6 nm) and deposited onto an ITO-coated film (21 nm) glass window. The LSPR shift is defined with respect to a reference which is the plasmonic sample before CO adsorption. Each point is measured after 30 min (thermal equilibrium). The accuracy of the wavelength measurements in the LSPR response is 0.01 nm (error bars).

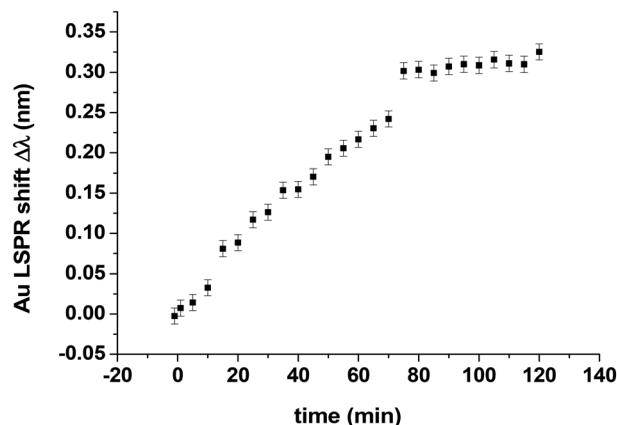


**Fig. 8** Experimental Au LSPR shift versus time at  $T = 418$  K for Pt<sub>10</sub> clusters deposited on Au disks ( $h = 17.5$  nm,  $p = 300$  nm,  $d = 140$  nm) covered with a SiO<sub>2</sub> layer (6 nm) and deposited onto an ITO-coated film (21 nm) glass window. The LSPR shift is defined with respect to a reference which is the plasmonic sample before O<sub>2</sub> adsorption. The accuracy of the wavelength measurements in the LSPR response is 0.01 nm (error bars).

We clearly observed two different regimes during oxygen adsorption: the first with an almost linear  $\Delta\lambda$  increase (slope =  $0.003 \text{ nm min}^{-1}$ ) and a plateau after 70 min corresponding to a redshift of  $\Delta\lambda_{\text{max}} \sim 0.3$  nm which is definitely larger than those measured on 3 nm Pt cubes ( $\Delta\lambda_{\text{max}} = 0.2$  nm).<sup>7</sup> We can therefore assume that we have both oxygen chemisorption and oxidation of Pt<sub>10</sub> clusters until reaching a regime where  $\Delta\lambda_{\text{max}}$  remains constant and the Pt<sub>10</sub> clusters are fully oxidized. The catalytic activity of Pt clusters depends on their oxidation state, so it's important to monitor this oxidation state and INPS is useful for this purpose. Our result is comparable to the work of Langhammer *et al.*<sup>9</sup> who showed by INPS that oxidation of Pd nanoparticles caused a redshift and a complete oxidation in 100 ppm O<sub>2</sub> (corresponding to an O<sub>2</sub> partial pressure of 10 Pa at atmospheric pressure). Ono *et al.*<sup>25</sup> studied the interaction of oxygen with Pt nanoparticles (sizes  $\leq 3.6$  nm) supported on SiO<sub>2</sub>/Si(001) and exposed to oxygen plasma at room temperature. From XPS measurements, they show that at low atomic oxygen exposures, chemisorbed species were detected on the samples, whereas higher exposures resulted in complete oxidation of the Pt nanoparticles. Up to 450 K, they found that the content of PtO in the nanoparticles increases, while that of PtO<sub>2</sub> decreases, and the metallic Pt remains fairly constant. PtO is stable up to 450 K, after which the decrease in its signal is accompanied by an increase in the metallic Pt content. In addition, for identical atomic oxygen exposures, a decrease in NP size was found to favour their ability to form oxides. C. Dessal *et al.*<sup>26</sup> have followed the possible mobility/redispersion of Pt clusters under O<sub>2</sub> by E-STEM under 130 Pa O<sub>2</sub>. The clusters are quasi-immobile under O<sub>2</sub> between RT and 800 °C. DFT calculations show that under these conditions, the Pt<sub>13</sub> clusters are strongly oxidized (from 1.5 to 1.8 O per Pt atom) and remain strongly bonded to the support.

After the oxygen adsorption experiment, the oxygen is evacuated from the reactor kept at 418 K and CO is introduced at a pressure of 44 Pa to try to remove and reduce the oxygen adsorbed on the Pt clusters. In other words, to investigate if the situation was reversible that is to say CO could reduce the oxidized Pt<sub>10</sub> clusters, thereby restoring their metallic nature. Fig. 9 shows the evolution of the shift  $\Delta\lambda$  as a function of time. During the first 10 minutes,  $\Delta\lambda$  decreases rapidly and finally remains constant at a value of about  $-0.1$  nm. This rapid decrease is explained by the removal of oxygen atoms from the Pt clusters in forming CO<sub>2</sub>. The minimum value of  $\Delta\lambda$  after 20 minutes cannot be directly compared with those measured for CO adsorption experiments at  $P_{\text{CO}}$  saturation (Fig. 7) because the reference values for the shift measurements are not the same. With the clean Pt clusters as a reference, a larger  $\Delta\lambda$  value is expected. This observation can be understood by two possible explanations: (1) the Pt clusters are not completely reduced after CO exposure and (2) the Pt<sub>10</sub> clusters initially 2D become 3D during the reaction of oxygen atoms with CO to form CO<sub>2</sub>, and as a result, the number of surface Pt atoms decreases, *i.e.* the maximum number of CO adsorption sites is lower than that for the initial 2D clusters. The second explanation is more likely since a recent report by Yin *et al.*<sup>17</sup> In fact, this work on the CO oxidation of Pt<sub>10</sub> clusters on alumina shows (by STM measurements) that there is no coalescence during the reaction, but the initial 2D cluster shape becomes 3D. It is very likely that the same phenomenon occurs for Pt<sub>10</sub> supported on silica.

### 3.3 CO oxidation

The CO oxidation experiment is performed by introducing a mixture of pure CO and O<sub>2</sub> gases with different compositions into the reactor at 418 K, defined by  $X_{\text{CO}} = P_{\text{CO}}/(P_{\text{CO}} + P_{\text{O}_2})$ . The

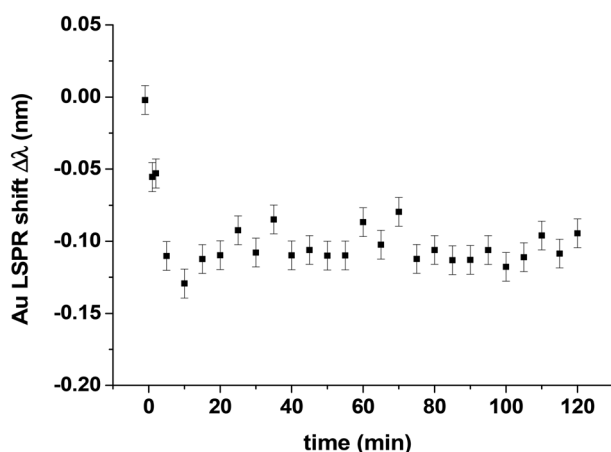


Fig. 9 Experimental Au LSPR shift *versus* time at  $T = 418$  K and  $P_{\text{CO}} = 44$  Pa for Pt<sub>10</sub> clusters deposited on Au disks ( $h = 17.5$  nm,  $p = 300$  nm,  $d = 140$  nm) covered with a SiO<sub>2</sub> layer (6 nm) and deposited onto an ITO-coated film (21 nm) glass window. The LSPR shift is defined with respect to a reference which is the plasmonic sample before CO adsorption. The accuracy of the wavelength measurements in the LSPR response is 0.01 nm (error bars).

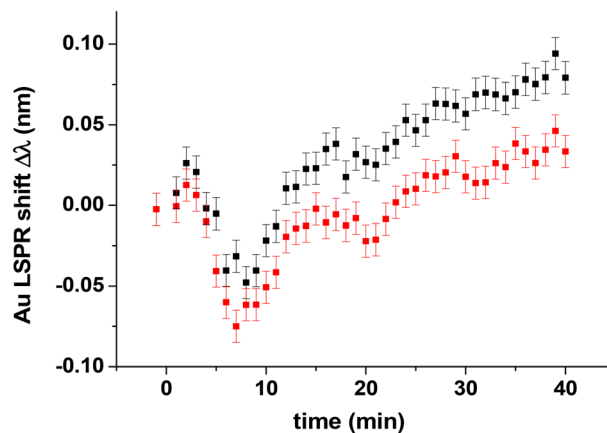


Fig. 10 Experimental Au LSPR shifts *versus* time at  $T = 418$  K for Pt<sub>10</sub> clusters deposited on Au disks ( $h = 17.5$  nm,  $p = 300$  nm,  $d = 140$  nm) covered with a SiO<sub>2</sub> layer (6 nm) and deposited onto an ITO-coated film (21 nm) glass window. The LSPR shift is defined with respect to a reference, which is the plasmonic sample before the introduction of CO and O<sub>2</sub> gases. Black points correspond to  $X_{\text{CO}} = 0.1$  and red points correspond to  $X_{\text{CO}} = 0.5$ . The accuracy of the wavelength measurements in the LSPR response is 0.01 nm (error bars).

LSPR shifts  $\Delta\lambda$  induced by the gas upon adsorption/reaction on the Pt<sub>10</sub> clusters were measured *versus* time (Fig. 10).

For both  $X_{\text{CO}}$  values (0.1 and 0.5) given in Fig. 10, we observed a decrease of  $\Delta\lambda$  and then a linear increase with a slope of  $0.003 \text{ nm min}^{-1}$ , similar to the slope measured for pure oxygen adsorption (Fig. 8). The two decreases of  $\Delta\lambda$  during the first 25 minutes can be explained by taking into account Fig. S3,<sup>†</sup> where we observed that the variation of  $\Delta\lambda$  is non-linear when the temperature decreases and linear when the temperature increases. So if we subtract the sensitivity ( $0.02 \text{ nm K}^{-1}$ ) times the sample temperature variation from the  $\Delta\lambda$  curve, we still have a negative  $\Delta\lambda$  variation artefact at  $t = 7$  min and  $t = 20$  min. The final  $\Delta\lambda$  value (0.08 nm) is greater for  $X_{\text{CO}} = 0.1$  (black points) than for  $X_{\text{CO}} = 0.5$  (red points), indicating a more oxygen-rich adsorbed layer associated with the lower  $X_{\text{CO}}$  value. At  $X_{\text{CO}} = 0.5$ , we measure  $\Delta\lambda = +0.03$  nm, superior to the value obtained on Pt nanocubes<sup>7</sup> ( $\Delta\lambda = -0.17$  nm). This indicates that we are in the O-rich regime on Pt<sub>10</sub> clusters, whereas on Pt nanoparticles, we were in the CO-rich regime. This is due to the fact that the CO/Pt<sub>10</sub> interaction is weaker than the interaction of CO with 3 nm Pt cubes.

## 4. Conclusion

The adsorption of CO, oxygen and CO oxidation on size-selected Pt<sub>10</sub> clusters were studied by indirect nanoplasmonic sensing (INPS) in the pressure range 1–100 Pa at 418 K. Regarding CO adsorption, we could observe a blueshift in the LSPR response, independent of the initial CO pressure, ranging from 1.1 Pa to 28 Pa. We observed a plateau at approximately  $\Delta\lambda = -0.1$  nm at  $P_{\text{CO}} > 2.7$  Pa, indicating saturation of



CO adsorption on Pt<sub>10</sub> clusters. This blue-shift is lower than that observed in our previous work on nanometer-size cubic Pt particles, probably because in Pt<sub>10</sub> clusters there are fewer Pt surface atoms per Au disk.

For oxygen, we clearly observed two different regimes during oxygen adsorption: the first with an almost linear  $\Delta\lambda$  increase and a plateau after 70 min corresponding to a redshift of  $\Delta\lambda_{\text{max}} \sim 0.3$  nm, which is definitely greater than those measured on 3 nm Pt cubes. We can therefore assume that we have both oxygen chemisorption and oxidation of the Pt<sub>10</sub> clusters until we reach a regime where  $\Delta\lambda_{\text{max}}$  remains constant and the Pt<sub>10</sub> clusters are completely oxidized. Our results are confirmed by literature work. The catalytic activity of Pt clusters depends on their oxidation state, so it's important to monitor this oxidation state and INPS is useful for this purpose. Demirdjian *et al.* have shown that chemisorption induces for Pt nanocubes an LSPR blueshift for CO and a redshift for oxygen; they have also shown that this behaviour is correlated with work function measurements found in the literature.<sup>7</sup>

CO oxidation was performed for  $X_{\text{CO}} = 0.1$  and  $X_{\text{CO}} = 0.5$ , and we observed a decrease of  $\Delta\lambda$  and then a linear increase, similar to the slope measured for pure oxygen adsorption. The final  $\Delta\lambda$  value (0.08 nm) is greater for  $X_{\text{CO}} = 0.1$  than for  $X_{\text{CO}} = 0.5$ , indicating a more oxygen-rich adsorbed layer associated with the lower  $X_{\text{CO}}$  value. At  $X_{\text{CO}} = 0.5$ , we measured  $\Delta\lambda = +0.03$  nm, superior to the value obtained on Pt nanocubes ( $\Delta\lambda = -0.17$  nm). This indicates that we are in the O-rich regime on Pt<sub>10</sub> clusters, whereas on Pt nanoparticles we were in the CO-rich regime. This is due to the fact that the CO/Pt<sub>10</sub> interaction is weaker than the interaction of CO with 3 nm Pt cubes.

This study demonstrates the applicability of indirect nanoplasmonic sensing as a highly sensitive method that allows the study of the adsorption and co-adsorption of CO and O<sub>2</sub> on samples with ultrasmall loadings of catalytic metal, here on the example of size-selected Pt<sub>10</sub> clusters applied at sub-monolayer coverage, as well as to monitor CO oxidation on these clusters along with the evolution of the oxidation state of Pt and the stability of these particles. This approach opens new ways towards the understanding of the nature and function of matter in the still largely unexplored subnanometer size regime where propensities may abruptly alter after changing the particle size by a single atom.

## Data availability

The data supporting this article have been included as part of the ESI.†

## Conflicts of interest

There are no conflicts to declare.

## Acknowledgements

Nanofabrication processes were performed in the PLANETE cleanroom facility (CINaM, Marseille), a part of the Renatech + French National network.

The authors sincerely thank the laboratory electron microscopy service and its agents (A. Altié and D. Chaudanson) for assisting them in SEM observations.

M. V. and S. V. acknowledge the assistance provided by the Advanced Multiscale Materials for Key Enabling Technologies project, supported by the Ministry of Education, Youth, and Sports of the Czech Republic. Project No. CZ.02.01.01/00/22\_008/0004558, co-funded by the European Union. M. V. and S. V. would like to thank the Argonne National Laboratory for facilitating the use of the cluster synthesis equipment for this study.

## References

- 1 C. R. Henry, *Surf. Sci. Rep.*, 1998, **31**, 235–326.
- 2 G. A. Somorjai, R. L. York, D. Butcher and J. Y. Park, *Phys. Chem. Chem. Phys.*, 2007, **9**, 3500–3513.
- 3 E. Ozensoy, D. C. Meier and D. W. Goodman, *J. Phys. Chem. B*, 2002, **106**, 9367–9371.
- 4 J. Wang, A. Ouvrard, W. Zheng, S. Carrrez, A. Ghalgaoui and B. Bourguignon, *Phys. Chem. Chem. Phys.*, 2023, **25**, 10845–10852.
- 5 L. Nguyen, F. F. Tao, Y. Tang, J. Dou and X. J. Bao, *Chem. Rev.*, 2019, **119**, 6822–6905.
- 6 E. M. Larsson, C. Langhammer, I. Zoric and B. Kasemo, *Science*, 2009, **326**, 1091–1094.
- 7 B. Demirdjian, I. Ozerov, F. Bedu, A. Ranguis and C. R. Henry, *ACS Omega*, 2021, **6**, 13398–13405.
- 8 C. Langhammer, E. M. Larsson, B. Kasemo and I. Zoric, *Nano Lett.*, 2010, **10**, 3529–3538.
- 9 C. Langhammer and E. M. Larsson, *ACS Catal.*, 2012, **2**, 2036–2045.
- 10 S. Liu, A. Susarrey-Arce, S. Nilsson, D. Albinsson, L. Hellberg, S. Alekseeva and C. Langhammer, *ACS Nano*, 2019, **13**, 6090–6100.
- 11 K. Wettergren, A. Hellman, F. Cavalca, V. P. Zhdanov and C. Langhammer, *Nano Lett.*, 2015, **15**, 574–580.
- 12 E. C. Tyo and S. Vajda, *Nat. Nanotechnol.*, 2015, **10**, 577–588.
- 13 R. Jin, G. Li, S. Sharma and Y. Li, *Chem. Rev.*, 2021, **121**, 567–648.
- 14 N. Zaman, G. Roberts, J. von der Heyde and A. Kara, *Surf. Sci.*, 2023, **733**, 122290.
- 15 S. Nigam and C. Majumder, *Appl. Surf. Sci.*, 2021, **547**, 149160.
- 16 B. Demirdjian, I. Ozerov, F. Bedu, A. Ranguis and C. R. Henry, *Chem. Phys. Lett.*, 2024, **837**, 141063.
- 17 C. Yin, F. R. Negreiros, G. Barcaro, A. Beniya, L. Sementa, E. C. Tyo, S. Bartling, K.-H. Meiwes-Broer, S. Seifert, H. Hirata, N. Isomura, S. Nigam, C. Majumder, Y. Watanabe, A. Fortunelli and S. Vajda, *J. Mater. Chem. A*, 2017, **5**, 4923–4931.





- 18 C. Yin, E. Tyo, K. Kuchta, B. von Issendorff and S. Vajda, *J. Chem. Phys.*, 2014, **140**, 174201.
- 19 I. Ragheb, M. Braik, S. Lau-Truong, A. Belkhir, A. Rummyantseva, S. Kostcheev, P. M. Adam, A. Chevillot-Biraud, G. Levi, J. Aubard, L. Boubekeur-Lecaue and N. Felidj, *Nanomaterials*, 2020, **10**, 2201.
- 20 C. Langhammer, E. M. Larsson, B. Kasemo and I. Zoric, *Nano Lett.*, 2010, **10**, 3529–3538.
- 21 W.-F. Wu and B.-S. Chiou, *Appl. Surf. Sci.*, 1993, **68**, 497–504.
- 22 M. P. Collings, V. L. Frankland, J. Lasne, D. Marchione, A. Rosu-Finsen and M. R. S. McCoustra, *Mon. Not. R. Astron. Soc.*, 2015, **449**, 1826–1833.
- 23 J. S. Agustsson, U. B. Arnalds, A. S. Ingason, K. B. Gylfason, K. Johnsen, S. Olafsson and J. T. Gudmundsson, *J. Phys.: Conf. Ser.*, 2008, **100**, 082006.
- 24 R. E. Winans, S. Vajda, B. Lee, S. J. Riley, S. Seifert, G. Y. Tikhonov and N. A. Tomczyk, *J. Phys. Chem. B*, 2004, **108**, 18105–18107.
- 25 L. K. Ono, J. R. Croy, H. Heinrich and B. R. Cuenya, *J. Phys. Chem. C*, 2011, **115**, 16856–16866.
- 26 C. Dessal, A. Sangnier, C. Chizallet, C. Dujardin, F. Morfin, J.-L. Rousset, M. Aouine, M. Bugnet, P. Afanasiev and L. Piccolo, *Nanoscale*, 2019, **11**, 6897–6904.

